Peer-reviewed version available at Remote Sens. 2018, 11, 50; doi:10.3390/rs11010050

Technical Note

Arctic sea ice surface roughness derived from multi-angular reflectance satellite imagery

Anne W. Nolin [1]

1 Department of Geography, University of Nevada, Reno, NV, 97331-5503, USA; anne.nolin@gmail.com
* Correspondence: anolin@unr.edu

Abstract: Sea ice surface roughness affects ice-atmosphere interactions, serves as an indicator of ice age, shows patterns of ice convergence and divergence, affects the spatial extent of summer melt ponds, and ice albedo. We have developed a method for mapping sea ice surface roughness using angular reflectance data from the Multi-angle Imaging SpectroRadiometer (MISR) and lidar-derived roughness measurements from the Airborne Topographic Mapper (ATM). Using an empirical data modeling approach, we derived estimates of Arctic sea ice roughness ranging from centimeters to decimeters meters within the MISR 275-m pixel size. Using independent ATM data for validation, we find that histograms of lidar and multi-angular roughness values are nearly identical for areas with roughness <20 cm but that for rougher regions, the MISR-derived roughness has a narrower range of values than the ATM data. The algorithm is able to accurately identify areas that transition between smooth and rough ice. Because of its coarser spatial scale, MISR-derived roughness data have a variance of about half that ATM roughness data.

Keywords: sea ice; surface roughness; remote sensing; MISR

1. Introduction

Sea ice roughness is created by surface-atmosphere interactions, ice motion, and ice surface melt. Roughness caused by ice motion depends on wind speed and direction, ocean currents, and coastline interactions [1]. Seasonal snow deposition on sea ice tends to smooth the surface and reduces the aerodynamic roughness length [2,3] while subsequent wind erosion and redeposition of blowing snow creates sastrugi and snow dunes on the ice [3,4]. Sea ice roughness enhances atmospheric boundary layer turbulence thereby affecting turbulent energy transfer and boundary layer height [4–6]. The spatial extent of spring season melt ponds on sea ice, as governed by surface roughness, is a skillful predictor of late summer ice extent [7]. This is because the crevices present in rough ice tend to confine surface meltwater whereas smoother ice allows surface melt to spread laterally. Because meltponds have a much lower albedo than sea ice, spatially extensive meltponds lead to lower albedo sea ice and a stronger ice-albedo positive feedback [8–10]. Thus, roughness is an important diagnostic indicator of sea ice processes and a valuable prognostic indicator of Arctic albedo.

Remote sensing is a valuable tool for assessing the state of sea ice over space and time. However, sea ice surface roughness is a source of uncertainty in remote sensing and itself has been a challenging parameter to retrieve. Satellite remote sensing of sea ice is one of the oldest remote sensing records available [ref] but surface topography measurements (e.g. radar, scatterometry, laser altimeter) have been too coarse to adequately characterize spatial and temporal changes in sea ice roughness. Airborne lidar data over sea ice provides fine scale spatial resolution data over sea ice but the overall spatial and temporal coverage is sparse.

In previous work, Nolin et al. [11] described initial success in characterizing ice surface roughness by combining images from the 60^{o} forward viewing and 60^{o} aft viewing cameras from NASA's Multi-angle Imaging SpectroRadiometer (MISR). This angular reflectance composite formed the 'normalized difference angular index' (NDAI), which compares the relative amount of backward to forward scattering of sunlight. It has been shown that the NDAI is a good proxy for

surface roughness and can be used to discriminate between rough bare ice and snowcover, especially when paired with observational data acquired from aircraft over sites such as widely studied Jakobshavn Isbræ on the western margin of the Greenland ice sheet. In that work and here as well, roughness is defined as the root mean square (RMS) of deviations of measured surface elevations from a fitted plane of a specified extent, in this case an 80-m "platelet" from the Airborne Topographic Mapper (ATM) lidar instrument as depicted in Figure 1.

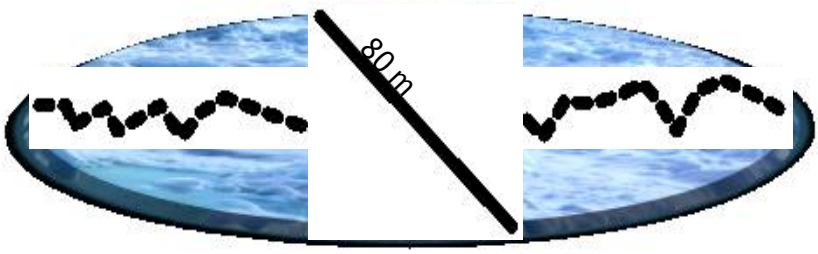

Figure 1. Depiction of sea ice surface roughness in an ATM 80-m platelet.

Although a positive correlation between NDAI and roughness clearly exists, this initial approach was fundamentally limited by its qualitative nature. While airborne lidar provides excellent spatial resolution and the ability to map centimeter to meter-scale changes in roughness, airborne data lack spatial coverage and regular repeat frequency. The advantage of employing a satellite-based retrieval of roughness is that it provides good coverage over remote sea ice regions and has the potential to map changes seasonal changes in sea ice roughness. Therefore, the overarching goal of this project was to develop a satellite-based technique for quantitative mapping of sea ice roughness with adequate quantitative precision to assess surface roughness characteristics across the physically relevant scales, from centimeters to meters and with the potential for implementing the technique over large areas.

Previous satellite efforts to map sea ice surface roughness has employed passive microwave, radar altimetry, scatterometry, and laser altimetry. Passive microwave has a footprint of 6-25 km, so coverage is excellent but the coarse spatial resolution doesn't provide process scale information. Cryosat-2 radar altimetry [12] offers higher spatial resolution (1650m x 380m) but surface roughness is determined by least-squares fitting of the radar return waveform [13]and can be confounded by backscatter angle. Scatterometry is sensitive to sea ice roughness though roughness is only one of several factors that simultaneously affect backscatter [14,15]. Laser altimetry measures sea ice elevations with a footprint of 70m and 170m spacing so spatial coverage is not continuous; elevation retrievals are affected by roughness within each footprint so it remains challenging to provide process-scale information on sea ice roughness [16].

2. Methodology

2.2. Description of the Multi-angle Imaging SpectroRadiometer (MISR)

Launched on NASA's Terra satellite in 1999, MISR views the amount of sunlight scattered in 9 along-track directions and at 4 wavelengths (blue, green, red, and near infrared) [17]. The near-polar, sun-synchronous orbit of MISR takes 16 days, to map Earth's surface up to a latitude of 83°. Each of MISR's 233 orbital paths contains a swath of data divided into 180 blocks each of which is 360 km wide. The 9 MISR cameras are labeled Df, Cf, Bf, Af, An, Aa, Ba, Ca, and Da. The initial letter (A, B, C, D) of each camera denotes the focal length and viewing angle of the camera. The viewing angles for the off-nadir A, B, C, and D cameras are 26.1°, 45.6°, 60.0°, and 70.5°, respectively, relative to the horizontal plane on the Earth's surface. The lowercase letters (f, n, a) denote whether the camera is looking forward, nadir, or aftward, respectively.

2.4. Calibrating and mosaicking multiangular reflectance data to create roughness maps

The overall approach for creating quantitative maps of surface roughness entails using multiangular reflectance and calibrating these data with measurements of ice sheet surface roughness from airborne LiDAR data. Calibration is achieved by developing an empirical relationship between three angular reflectance quantities (reflectance values from MISR Ca, Cf, and An cameras) and the ATM roughness data. These data are the basis for a four-dimensional (4-D) model that assigns roughness values to MISR data, based on the empirical relationship between angular reflectance and measured ice sheet surface roughness. There are four main steps in developing maps of ice sheet surface roughness: (1) preprocessing the data; (2) building the 4-D model; (3) applying the model to new MISR data; and (4) spatially aggregating and mosaicking the data to create roughness maps. We also assess the model skill using a variety of metrics.

2.5. Data and data preprocessing

We begin with MISR top-of-atmosphere (TOA) radiance data (ML1B2E), which has the nine MISR cameras geometrically rectified to the Earth ellipsoid. Based on previous work by Nolin et al. [11] and Nolin and Payne [18], we use the red band from the Cf, Cn, and An cameras to optically characterize the forward and backward scattering characteristics of the sea ice surface. The relative amount of backward scattering to forward scattering is an indication of the relative surface roughness.

To assign a quantitative roughness value to the MISR angular reflectance data, we require measurements of sea ice surface roughness over a wide range of roughness values and at a spatial scale that is comparable to the MISR 275-m pixel size. For this purpose, we used roughness data from the Airborne Topographic Mapper (ATM) IceBridge ATM L2 Icessn Elevation, Slope, and Roughness, Version 2 [19]. ATM is a conical scanning airborne laser altimeter that measures the distance from the aircraft to the topographic surface below using a 532-nm pulsed laser [20]. For this study, we used ATM data acquired with the instrument mounted on either the NASA P3 or DC8 aircraft. The instrument flies at a nominal altitude of 500-750 m, using a scanner angle of 22° with a laser footprint of ~1 m, a footprint spacing of ~3 m, horizontal accuracy of 74 cm, and vertical precision of 3 cm [20]. The icessn-processed ATM data have been resampled from the original high-volume elevation data set by fitting ~80 m diameter overlapping "platelets" along the flight line using along-track and cross-track slopes and then computing the average and root mean square (RMS) deviation of all elevation points within each platelet to yield values for average elevation and roughness, respectively.

Using the geolocation data and time tags from the ATM data we identify the corresponding MISR image closest in time (±1 day) of the ATM overflight. The interval of ±1 day from the ATM flight path is used because there may not have been cloud-free, ATM-coincident data. Since the ATM data acquisitions are flown under clear sky conditions, the corresponding MISR reflectance data must also be cloud-free. To identify and remove MISR reflectance data that are contaminated by clouds, we use the MISR Angular Signature Cloud Mask (ASCM, MIL2TCCL) product [21]. Specifically, we use the "high confidence clear" data from this cloud mask product. We note that the cloud masks over sea ice tend to exclude smooth snow-covered ice because of the similarity to clouds. Thus, for the most accurate calibration we relied on both the cloud mask and careful visual checks. If both the visual check and the ASCM cloud mask indicate the presence of a cloud, then we exclude both the MISR reflectance and the ATM surface roughness data for those locations.

Because the MISR footprint is larger than that of the ATM icessn-processed roughness data, there are multiple ATM roughness values within each MISR pixel. The latitude and longitude of each ATM roughness value are matched to the closest MISR pixel using the pixel center coordinates. The ATM roughness values within each corresponding MISR pixel are then averaged and we recorded the average roughness, standard deviation, and number of ATM values. The average and number of ATM values are later used in a weighting function described in the following section.

2.6. Building the 4-D Surface Roughness Model

In the roughness model, each set of three MISR reflectance values (from the An, Ca, and Cf cameras) has a corresponding ATM-derived roughness value. We refer to this as a four-dimensional (4-D) model. In constructing the empirical relationship between the angular reflectance values and lidar-derived surface roughness values, we begin by compositing the ATM icessn-processed roughness values located within a MISR pixel and assigning the average to the MISR pixel. The average, standard deviation, and number of ATM roughness values used in the calculation are retained for subsequent use. This average roughness is then the modeled roughness for the MISR pixel.

We use a nearest-neighbor approach to assign a surface roughness value for each triad of An, Ca, Cf reflectance values. Thus, we needed to determine the prediction radius within which a roughness value can be determined. Using all the 2013 and 2016 ATM roughness data and corresponding MISR data, we computed an optimal prediction radius, r_{pred}. We varied r_{pred} to determine whether there exists an optimal r_{pred} value that gives the highest correlation with the "true" roughness (as measured by the ATM). Note that not all MISR-ATM model data points will have surrounding data points within the prediction radius. As r_{pred} is increased, there is a greater chance that there will be a roughness prediction value within the search radius but there is also a greater chance that the predicted roughness will have a lower correlation with the actual roughness of the point to be modeled. So, another important parameter is the coverage, *C*, of the ATM model as a function of the prediction radius. Coverage is defined as the number of MISR pixels within the prediction radius that can be assigned a roughness value (n_{pred}) relative to the total number of valid MISR pixels in the image (N_{MISR}):

$$C = \frac{n_{pre}(r_{pred})}{N_{MISR}} \quad (1)$$

It is desirable to maximize *C* but as the prediction radius is increased, there is a greater chance that the predicted roughness will have a lower correlation with the actual roughness of the point to be modeled. This is important because for nearest neighbor classification a small radius could result in no corresponding roughness value and a large radius would mean that a value could have an excessively wide a range of roughness values.

We computed the average of the roughness values within each progressively larger concentric sphere and then computed the correlation between the "true" ATM-measured roughness value and the estimated roughness value for each value of r_{pred}. This was performed for each of the >1,000,000 pixels used to generate the 4-D model. The optimal radius was determined to be 0.025. Units are reflectance.

Using the 0.025 value for r_{pred}, we then assign a roughness value to each new MISR pixel. The nearest-neighbor method was used to find those roughness values in the model data cloud closest to that of the new MISR pixel. The location of each point within the local prediction radius is determined by the following constraint:

$$r_{pred} \leq \sqrt{(\mathrm{Cf}_m - \mathrm{Cf}_p)^2 + (\mathrm{Ca}_m - \mathrm{Ca}_p)^2 + (\mathrm{An}_m - \mathrm{An}_p)^2} \quad (2)$$

where, Cf_m, Ca_m, and An_m are the x, y, z coordinates of the model data point and Cf_p, Ca_p, and An_p are the x, y, z coordinates of the prediction data point. Because in creating the model, we average the multiple ATM roughness values within a MISR pixel, not all model points are created with the same number of ATM roughness values. To account for this, a weighting scheme is used that is based on the number of ATM roughness values that comprise each point in the data model. The weighted average roughness value (μ_w) of the prediction data point is:

$$\mu_w = \frac{\sum_{i=1}^{m} n_i x_i}{\sum_{i=1}^{m} n_i} \quad (3)$$

where, μ_w= weighted average roughness predicted for the new MISR pixel, m = total number of model data points within r_{pred}, n_i = number of ATM roughness values used to compute the roughness for that model data point, and x_i = model roughness values within r_{pred}

2.6. Applying the Model to New MISR Data

Next the 4-D model was used to assign a roughness value to every pixel in a new MISR sea ice image. Preprocessing of the MISR data is the same as with the MISR data used to construct the 4-D model: converting TOA radiance (from the Ca, Cf, and An cameras) to reflectance. The reflectance values are placed into the 4-D model space and, using r_{pred} = 0.025, each MISR roughness value is formulated as the weighted average of points within r_{pred}.

3. Results

3.1. Roughness Maps from MISR

The 4-D model described above was used to convert MISR reflectance data for all cloud-free MISR orbits during April-July 2013 and 2016 in the Arctic region extending from the Beaufort Sea to Ellesmere Island in the Canadian Archipelago. This region was selected because prior research showed this to be an important region of convergence and divergence [22] used that model to calibrate MISR reflectance data into roughness. Figure 2 shows the results of the MISR-derived surface roughness algorithm for a spring image (26 April 2016) and a summer image (15 July 2016). The spring image is almost entirely cloud-free. It shows an extensive area of relatively smooth sea ice with roughness values of mostly 12-20 cm. There is one very rough area of ice in the Greely Fiord of Ellesmere Island where there are ice roughness values exceeding 80 cm. In this region, the ice pack represents dynamic glacier ice that has flowed into the fiord and frozen in place. The summer image contains clouds in the center portion of the image. Focusing on the cloud-free southern part of the image the roughness image shows ice floes, ridges, cracks and other convergence-divergence features. As in the spring image, the largest values for ice roughness are found in Greely Fiord.

3.2 Assessment of Results

To assess the accuracy of the method, MISR-derived sea ice roughness values were compared with corresponding independent ATM roughness data, which had not been used to construct the 4-D model. Results were assessed for three categories: smooth (roughness < 20cm), rough (roughness > 20 cm), and smooth-rough transitions. Figures 3a-c show MISR-derived and ATM roughness values from a validation data set that used co-located MISR and ATM roughness data. As before, the MISR data acquisition was within ±1 day of the ATM overflight. The 80m ATM roughness values within each MISR pixels were averaged so that an individual ATM and MISR values could be compared. The validation data were from ATM overflight data during April-May 2016 and were selected to encompass smooth, rough, and smooth-rough transitions. Figure 3 and Table 1 show that for smooth ice, the mean values are virtually identical and the range and variance are also quite similar between MISR and ATM. This is not the case for rough ice where the mean values are close but the ATM has a much greater variance than MISR. Results for smooth-rough transitions show that the MISR roughness retrievals do a good job of tracking abrupt changes in roughness.

Preprints (www.preprints.org) | NOT PEER-REVIEWED | Posted: 22 October 2018 doi:10.20944/preprints201810.0484.v1

Peer-reviewed version available at Remote Sens. 2018, 11, 50; doi:10.3390/rs11010050

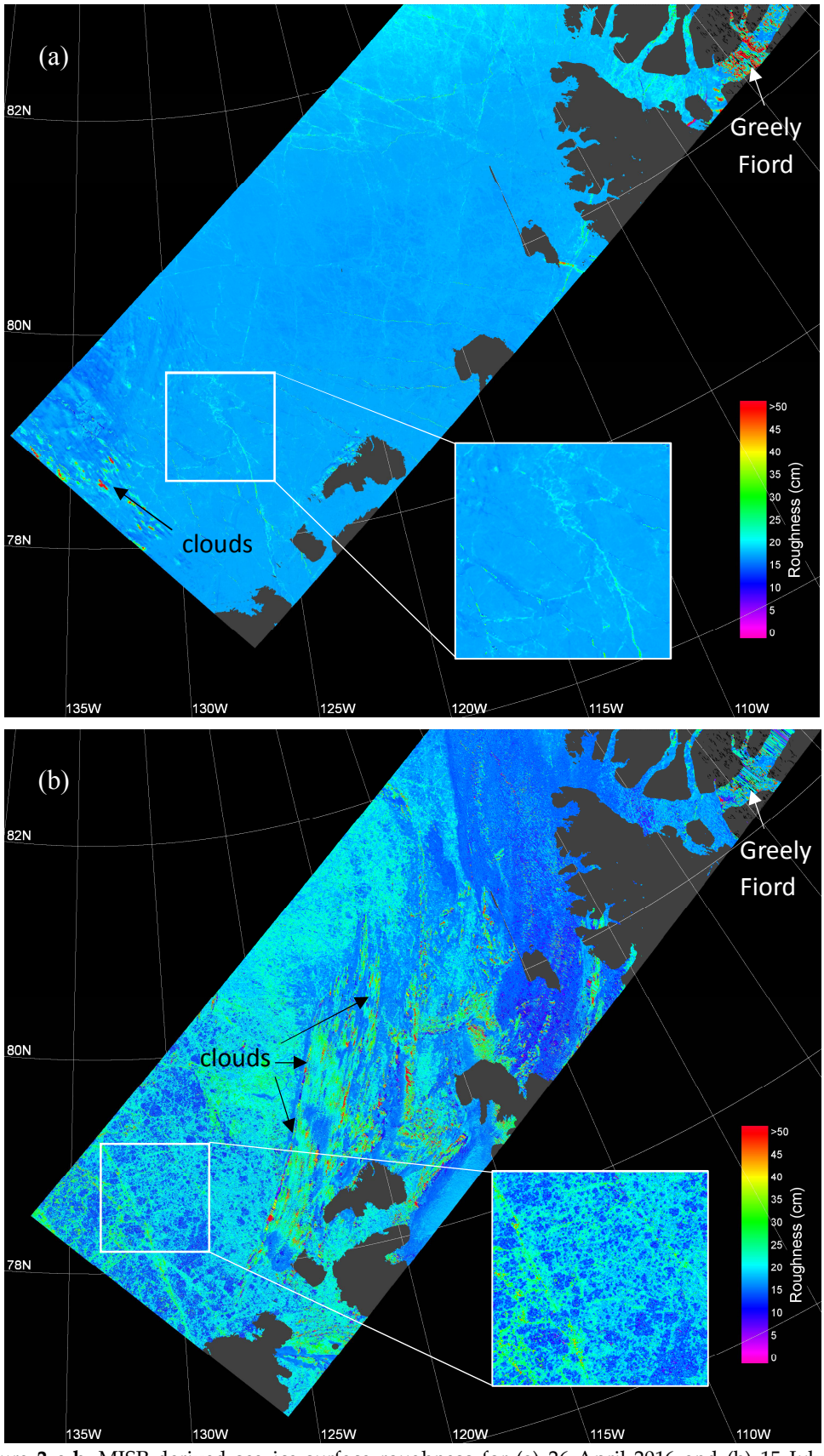

Figure 2 a-b. MISR-derived sea ice surface roughness for (a) 26 April 2016 and (b) 15 July 2016 (bottom). The Beaufort Sea region has been highlighted to show the seasonal changes in roughness. Clouds have not been masked and appear as rough streaks. The roughest ice in both images is in the Greely Fiord of Ellesmere Island (upper right of both images).

Preprints (www.preprints.org) | NOT PEER-REVIEWED | Posted: 22 October 2018 doi:10.20944/preprints201810.0484.v1

Peer-reviewed version available at Remote Sens. 2018, 11, 50; doi:10.3390/rs11010050

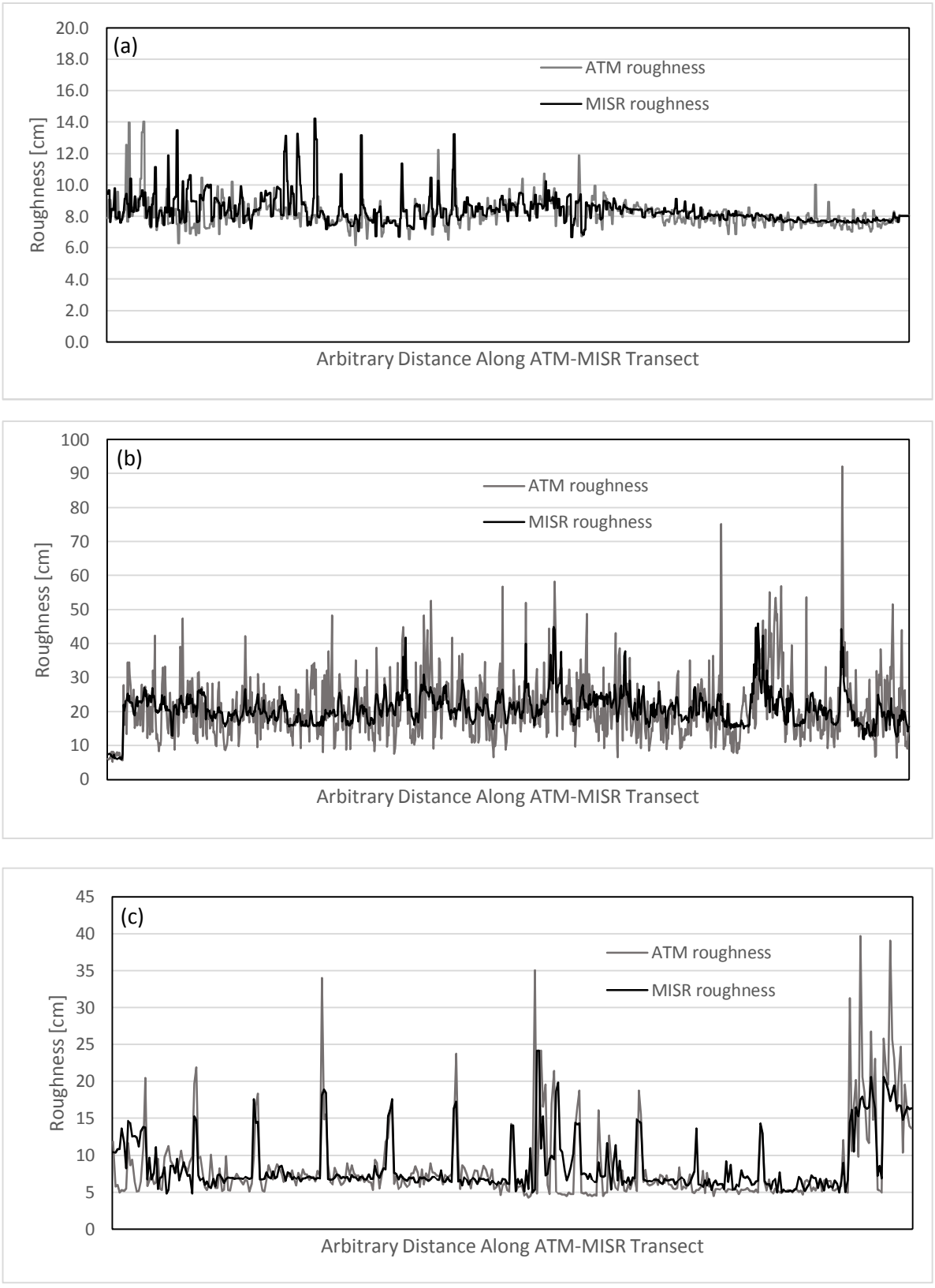

Figure 3 a-c. Comparison of ATM and MISR-derived sea ice surface roughness from April and May 2016. (a) smooth (<20 cm roughness); (b) rough (up to 100 cm roughness); and (c) smooth-rough transitions.

264 *2.2. Frequency Distributions*

265 A comparison of the frequency distributions of ATM and MISR-derived roughness values
266 indicates that the ability to accurately represent sea ice roughness depends on the magnitude of
267 roughness. We note that the values shown here are separate from the ATM and MISR data that were
268 used to construct the 4-D model used to derive MISR roughness. The frequency distributions shown
269 in Figure 4a demonstrate these differences for smooth, rough, and smooth-rough transitions. The
270 mean and median of ATM and MISR roughness values are nearly identical for smooth sea ice. For
271 rough ice (Figure 4b), the mean and median of ATM and MISR roughness values are also quite similar
272 but the range and variances are very different. The histogram in Figure 4c shows the characteristic
273 bimodal distribution for the smooth and rough sea ice areas. In the smooth-rough transition data,
274 most of the areas are smooth with short transitions to rough ice. The much smaller secondary mode
275 in Figure 4c shows this for both ATM and MISR-derived roughness values.

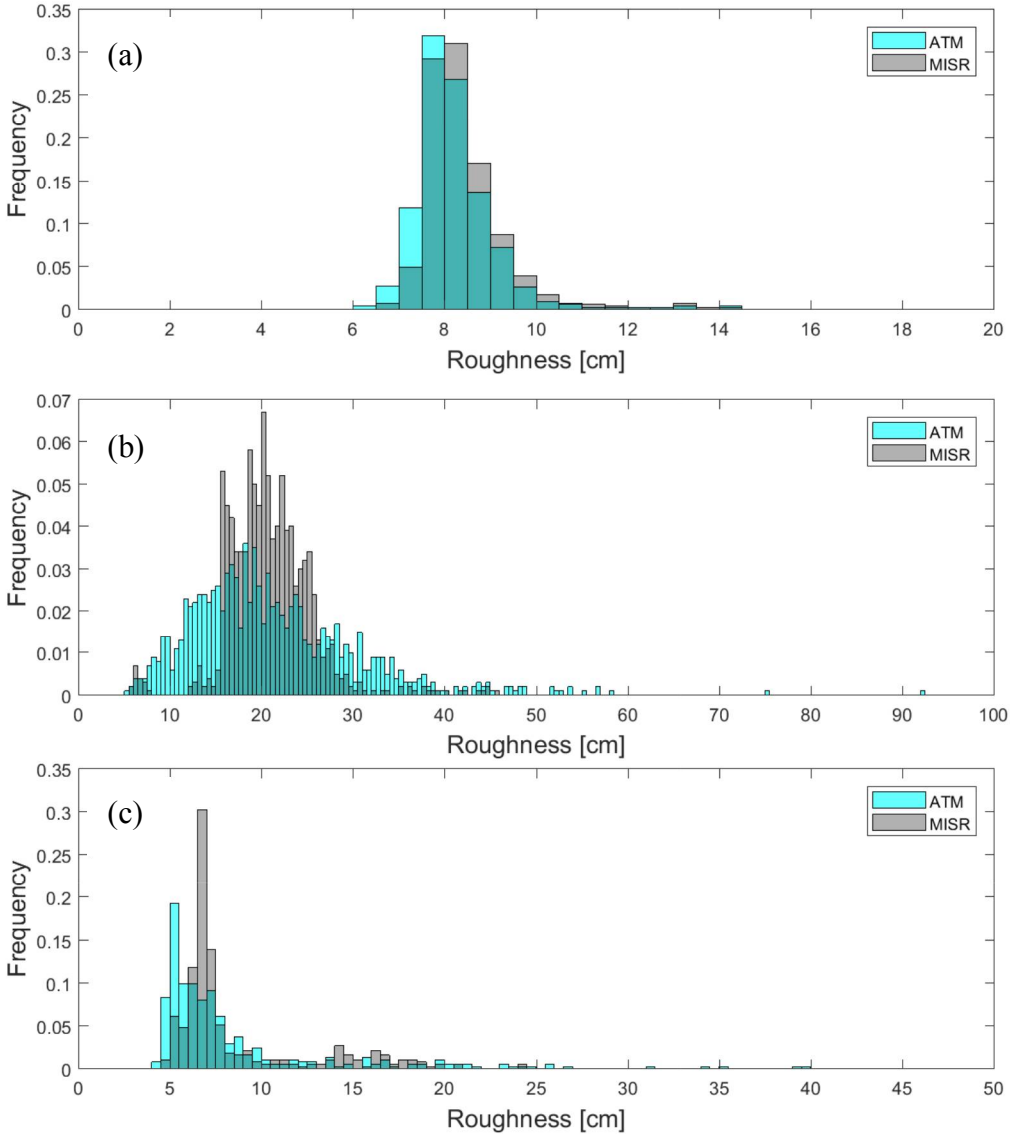

276
277
278

279 **Figure 4 a-c.** Histograms of ATM and MISR roughness frequency distributions for sea ice areas that
280 are (a) smooth (<20 cm roughness); (b) rough (up to 100 cm roughness); and (c) smooth-rough
281 transitions.

282

283

Table 1. ATM and MISR-derived roughness statistics for the histogram data in Figure 4.

Roughness type	Instrument	Mean roughness [cm]	Median roughness [cm]	Variance [cm²]	Maximum roughness [cm]	Minimum roughness [cm]
Smooth	ATM	8.2	8.0	0.9	14.1	6.2
	MISR	8.4	8.1	0.9	14.2	6.7
Rough	ATM	21.2	19.4	86.0	92.1	5.3
	MISR	20.8	20.4	23.1	46.0	6.0
Smooth-rough transitions	ATM	8.5	6.6	29.2	39.7	4.3
	MISR	8.6	6.9	14.5	24.2	4.8

4. Discussion

In the context of other methods to derive roughness, this work stands out because it provides spatially extensive roughness information at a horizontal scale of 275m and with vertical precision at centimeters to decimeters. This method is effective at mapping smooth ice, corresponding to thinner first year sea ice; rough ice, corresponding to thicker first year and multi-year sea ice; and ice with roughness that transitions between smooth and rough, corresponding to ice floes, surrounded by leads.

The MISR lower range of roughness values and smaller variance compared with ATM data is likely due to the differences in spatial resolution between MISR and ATM. Finer scale roughness features that appear in the ATM data are not resolved in a MISR pixel.

There are several sources of error to consider. First, the potential temporal offset of ±1 day between ATM data acquisition and a MISR overpass may result in a co-location error: a MISR pixel may not represent the same ice conditions as the ATM footprint. This type of error is relatively small in spring because cold temperatures tend to reduce ice motion at that time of year. A second source of error is the time period used in the calibration. If the 4D model is constructed using data from April-May, it may omit ice characteristics that are present later in the summer. Most ATM overflights occur in spring and it would be helpful to have a larger number of flights in summer and fall. Additional errors may enter from the 4D modeling process. Calculation of the prediction radius is optimized and results over multiple ice types show that it varies only a little; this would not contribute much to the full error budget. The largest challenge in the modeling process is identifying cloud-free MISR imagery. There is no adequate cloud mask that effectively identifies clouds over sea ice that can be used in an automated manner. Visual identification of clouds remains the best approach but is overly time consuming.

5. Conclusions

This multiangular remote sensing approach to mapping sea ice surface roughness appears to show great promise. These results demonstrate the ability to map changes in surface roughness at centimeter to decimeter scales in a 275-m MISR pixel. MISR-derived estimates of surface roughness suggest the ability to map features such as cracks, ridges, smooth snow, frozen leads, and meltponds. While this method is limited to cloud-free images during the sunlit season, it has the potential to map sea ice roughness during the critical spring season prior to meltpond formation. Calibration using the ATM lidar provides the key data to convert multiangular reflectance to quantifiable roughness estimates.

With further analysis this method could be used to map ice types based on roughness characteristics, to examine changes in the extent of first year and multiyear ice, and to map areas where leads are present. One could also analyze spatial patterns of sea ice roughness using frequency

analysis to better characterize convergence and divergence features. It is hoped that this approach can also be combined with new data to better train and constrain MISR-derived sea ice roughness. Future work will apply this method to a much larger region of the Arctic and over the full MISR record from 2000 to present. These sea ice roughness data can improve interpretation of sea ice thickness from spaceborne radar and laser altimeter instruments. Applying this new roughness method to the entire Arctic will benefit the Arctic sea ice science community and has potential for operational use in Arctic navigation.

Author Contributions: Conceptualization, A.N.; Methodology, A.N; Validation, A.N.; Formal Analysis, A.N.; Investigation, A.N.; Resources, A.N.; Data Curation, A.N.; Writing-Original Draft Preparation, A.N.; Writing-Review & Editing, A.N.; Visualization, A.N.; Supervision, A.N.; Project Administration, A.N.; Funding Acquisition, A.N.

Funding: This research was funded NASA/Jet Propulsion Laboratory Contract #1540933.

Acknowledgements: Eugene Mar for programming, the MISR team for their assistance.

Conflicts of Interest: The author declares no conflict of interest. Any brand name or companies in the paper are not endorsements. The funding sponsors had no role in the design of the study; in the collection, analyses, or interpretation of data; in the writing of the manuscript, and in the decision to publish the results.

References

1. Rothrock, D. A.; Thorndike, A. S. Geometric properties of the underside of sea ice. *J. Geophys. Res. Ocean.* **2018**, *85*, 3955–3963, doi:10.1029/JC085iC07p03955.
2. Fassnacht, S.R., Williams, M.W., Corrao, M. V. Changes in the surface roughness of snow from millimetre to metre scales. *Ecol. Complex.* **2009**, *6*, 221–229, doi:10.1016/j.ecocom.2009.05.003.
3. Déry, S. J.; Tremblay, L.-B. Modeling the Effects of Wind Redistribution on the Snow Mass Budget of Polar Sea Ice*. *J. Phys. Oceanogr.* **2004**, *34*, 258–271, doi:10.1175/1520-0485(2004)034<0258:MTEOWR>2.0.CO;2.
4. Sturm, M. Winter snow cover on the sea ice of the Arctic Ocean at the Surface Heat Budget of the Arctic Ocean (SHEBA): Temporal evolution and spatial variability. *J. Geophys. Res.* **2002**, *107*, 8047, doi:10.1029/2000JC000400.
5. Déry, S. J.; Taylor, P. A. Some aspects of the interaction of blowing snow with the atmospheric boundary layer. *Hydrol. Process.* **2018**, *10*, 1345–1358, doi:10.1002/(SICI)1099-1085(199610)10:10<1345::AID-HYP465>3.0.CO;2-2.
6. Smeets, C.; Duynkerke, P.; Vugts, H. Observed wind profiles and turbulence fluxes over an ice surface with changing surface roughness. *Boundary-Layer Meteorol.* **1999**, *92*, 99–121, doi:10.1023/A:1001899015849.
7. Schröder, D.; Feltham, D. L.; Flocco, D.; Tsamados, M. September Arctic sea-ice minimum predicted by spring melt-pond fraction. *Nat. Clim. Chang.* **2014**, *4*, 353.
8. Curry, J. A.; Schramm, J. L.; Ebert, E. E. Sea Ice-Albedo Climate Feedback Mechanism. *J. Clim.* **1995**, *8*, 240–247, doi:10.1175/1520-0442(1995)008<0240:SIACFM>2.0.CO;2.
9. Perovich, D. K.; Polashenski, C. Albedo evolution of seasonal Arctic sea ice. *Geophys. Res. Lett.* **2012**, *39*, 1–6, doi:10.1029/2012GL051432.
10. Landy, J. C.; Ehn, J. K.; Barber, D. G. Albedo feedback enhanced by smoother Arctic sea ice. *Geophys. Res. Lett.* **2015**, *42*, 10714–10720, doi:10.1002/2015GL066712.
11. Nolin, A. W.; Fetterer, F. M.; Scambos, T. A. Surface roughness characterizations of sea ice and ice sheets: case studies with MISR data. *IEEE Trans. Geosci. Remote Sens.* **2002**, *40*, 1605–1615, doi:10.1109/TGRS.2002.801581.
12. Shepherd, A.; Ivins, E. R.; Geruo, A.; Barletta, V. R.; Bentley, M. J.; Bettadpur, S.; Briggs, K. H.; Bromwich,

D. H.; Forsberg, R.; Galin, N.; Horwath, M.; Jacobs, S.; Joughin, I.; King, M. A.; Lenaerts, J. T. M.; Li, J.; Ligtenberg, S. R. M.; Luckman, A.; Luthcke, S. B.; McMillan, M.; Meister, R.; Milne, G.; Mouginot, J.; Muir, A.; Nicolas, J. P.; Paden, J.; Payne, A. J.; Pritchard, H.; Rignot, E.; Rott, H.; Sørensen, L. S.; Scambos, T. A.; Scheuchl, B.; Schrama, E. J. O.; Smith, B.; Sundal, A. V.; Van Angelen, J. H.; Van De Berg, W. J.; Van Den Broeke, M. R.; Vaughan, D. G.; Velicogna, I.; Wahr, J.; Whitehouse, P. L.; Wingham, D. J.; Yi, D.; Young, D.; Zwally, H. J. A reconciled estimate of ice-sheet mass balance. *Science (80-.).* **2012**, *338*, 1183–1189, doi:10.1126/science.1228102.

13. Kurtz, N. T.; Galin, N.; Studinger, M. An improved CryoSat-2 sea ice freeboard retrieval algorithm through the use of waveform fitting. *Cryosphere* **2014**, *8*, 1217–1237, doi:10.5194/tc-8-1217-2014.
14. Nghiem, S. V.; Rigor, I. G.; Perovich, D. K.; Clemente-Colón, P.; Weatherly, J. W.; Neumann, G. Rapid reduction of Arctic perennial sea ice. *Geophys. Res. Lett.* **2007**, *34*, 1–6, doi:10.1029/2007GL031138.
15. Remund, Q. P.; Long, D. G. A decade of QuikSCAT scatterometer sea ice extent data. *IEEE Trans. Geosci. Remote Sens.* **2014**, *52*, 4281–4290, doi:10.1109/TGRS.2013.2281056.
16. Kwok, R.; Cunningham, G. F.; Zwally, H. J.; Yi, D. ICESat over Arctic sea ice: Interpretation of altimetric and reflectivity profiles. *J. Geophys. Res. Ocean.* **2006**, *111*, doi:10.1029/2005JC003175.
17. Diner, D. J.; Asner, G. P.; Davies, R.; Knyazikhin, Y.; Muller, J.-P.; Nolin, A. W.; Pinty, B.; Schaaf, C. B.; Stroeve, J. New Directions in Earth Observing: Scientific Applications ofMultiangle Remote Sensing. *Bull. Am. Meteorol. Soc.* **1999**, *80*, 2209–2228, doi:10.1175/1520-0477(1999)080<2209:NDIEOS>2.0.CO;2.
18. Nolin, A. W.; Payne, M. C. Classification of glacier zones in western Greenland using albedo and surface roughness from the Multi-angle Imaging SpectroRadiometer (MISR). *Remote Sens. Environ.* **2007**, *107*, 264–275, doi:10.1016/j.rse.2006.11.004.
19. Studinger, M. IceBridge ATM L2 Icessn Elevation, Slope, and Roughness, Version 2 Available online: https://doi.org/10.5067/CPRXXK3F39RV (accessed on Jun 1, 2018).
20. Martin, C. F.; Krabill, W. B.; Manizade, S. S.; Russell, R. L.; Sonntag, J. G.; Swift, R. N.; Yungel, J. K. Airborne Topographic Mapper Calibration Procedures and Accuracy Assessment. *Nasa Tech. Memo.* **2012**, *TM–2012-21*.
21. Di Girolamo, L.; Wilson, M. J. A first look at band-differenced angular signatures for cloud detection from MISR. *IEEE Trans. Geosci. Remote Sens.* **2003**, *41*, 1730–1734, doi:10.1109/TGRS.2003.815659.
22. Kwok, R.; Schweiger, A.; Rothrock, D. A.; Pang, S.; Kottmeier, C. Sea ice motion from satellite passive microwave imagery assessed with ERS SAR and buoy motions. *J. Geophys. Res.* **1998**, *103*, 8191, doi:10.1029/97JC03334.